

Synergistic Fluorine...Sulfur Intra- and Intermolecular Interactions on Dopant-Free Hole Transport Material for Efficient and Stable Inverted Perovskite Solar Cells

Rui Li, Jiakang Zhang, Maning Liu,* Sri Kasi Matta, Jingshu Tian, Zhifeng Deng, Salvy P. Russo, Paola Vivo, Zhongmin Zhou,* and Haichang Zhang*

Designing dopant-free small-molecule hole transport materials (HTMs) with self-assembly behavior via noncovalent interactions is considered as one effective strategy to achieve high-performance inverted perovskite solar cells (PSCs). Herein, two donor- π bridge-donor (D- π -D) HTMs are presented, TPASF and TPAOF, containing 3,6-dimethoxythieno[3,2-b]thiophene as a core part with 3-fluoro-*N,N*-bis(4-(methylthio)phenyl)aniline and 3-fluoro-*N,N*-bis(4-methoxyphenyl)aniline as side group. The synergistic F...S dipole-dipole intra- and intermolecular interactions in TPASF drive the self-assembly of this molecule into a supramolecular nanofibrillar network, leading to high hole mobility, superior interfacial properties, and providing a good growth template for the perovskite layer atop. The corresponding dopant-free TPASF-based inverted devices exhibit a promising power conversion efficiency of 21.01% with a long T_{80} lifetime of ≈ 632 h under operational conditions. This work paves the way for the further development of new dopant-free self-assembled HTM designs for highly efficient and stable inverted PSCs.

value of 25.7%.^[1] To date, the majority of high-performance LHPSCs is fabricated in the n-i-p configuration with 4-*tert*-butyl pyridine (tBP)- and lithium bis(tri-fluoromethanesulfonyl)imide (Li-TFSI)-doped 2,2',7,7'-tetrakis(*N,N*-di-*p*-methoxyphenyl)amine)-9,9'-spirobifluorene (spiro-OMeTAD) as the hole transport material (HTM). Such hygroscopic and volatile dopants are, however, also a key factor for shortening the device lifespan.^[2–5] Recently, inverted p-i-n LHPSCs using dopant-free HTMs have attracted increasing attention, owing to the easier fabrication process, negligible hysteresis, and better compatibility with flexible substrates compared to their n-i-p counterparts.^[6–9] To replace the high-cost polymeric HTMs with low batch-to-batch reproducibility, for example, poly[bis(4-phenyl)(2,4,6-trimethylphenyl)amine] (PTAA),^[8,10] lately, dopant-free small-molecule HTMs have


been intensively investigated, in turn favoring cost-effective and scalable synthesis, low production discrepancy, low defect densities, and well-defined molecular structures.^[11–13] Among all the reported works on molecular engineering and interface functionalization of small-molecule HTMs,^[14–19] the best performance of noncommercial dopant-free small-molecule HTM-based inverted LHPSCs have approached 22%.^[20–22]

1. Introduction

Over the past decade, lead halide perovskite solar cells (LHPSCs) have been highlighted as one of the most attractive candidates among third-generation photovoltaics, due to their outstanding power conversion efficiencies (PCEs) that have demonstrated an unprecedentedly rapid increase up to the latest certified

R. Li, J. Zhang, J. Tian, Z. Zhou, H. Zhang
School of Polymer Science and Engineering & College of Chemistry and Molecular Engineering
Qingdao University of Science and Technology
Qingdao 266042, P. R. China
E-mail: zhouzm@qust.edu.cn; haichangzhang@qust.edu.cn

M. Liu, P. Vivo
Hybrid Solar Cells, Faculty of Engineering and Natural Sciences
Tampere University
FI-33014 Tampere, Finland
E-mail: maning.liu@tuni.fi

 The ORCID identification number(s) for the author(s) of this article can be found under <https://doi.org/10.1002/solr.202300031>.

© 2023 The Authors. Solar RRL published by Wiley-VCH GmbH. This is an open access article under the terms of the Creative Commons Attribution License, which permits use, distribution and reproduction in any medium, provided the original work is properly cited.

DOI: 10.1002/solr.202300031

S. K. Matta, S. P. Russo
Australian Research Council Centre of Excellence in Exciton Science
School of Science
RMIT University
Melbourne, Victoria 3000, Australia

S. K. Matta
JSPS International Research Fellow Center for Computational Sciences
University of Tsukuba
Tsukuba, Ibaraki 305-0006, Japan

Z. Deng
National and Local Joint Engineering Laboratory for Slag Comprehensive Utilization and Environmental Technology
School of Materials Science and Engineering
Shaanxi University of Technology (SNUT)
Hanzhong 723001, P. R. China

To construct high-hole-mobility small-molecule HTMs without dopants, the intrinsic low crystallinity of organic small-molecule materials should be tackled. Self-assembly via intermolecular non-covalent interactions is an attractive strategy for designing ordered small molecules with high carrier mobility.^[23,24] A considerable amount of effort has been devoted to control the assembly behavior by introducing the interatomic dipole moment interactions within and between the molecules such as $C=N-H$,^[25,26] $N-H\cdots O=C$,^[27] $C-H\cdots F$,^[28] and F (fluorine) $\cdots S$ (sulfur),^[29] wherein interactions generally comprise an electron-donor (D) atom and an electron-acceptor (A) atom. The fluorine atom is the smallest halogen atom with a strong electron-withdrawing ability, which can control the molecular planarity and also the highest occupied molecular orbital (HOMO) energy level. Song et al. synthesized a fluorinated dopant-free small-molecule HTM that can simultaneously increase the framework planarity and hole transport capability, leading to a maximum PCE of 20.2% for inverted devices.^[30] Very recently, Cheng et al. proposed a molecular assembly strategy by designing a linear organic small molecule, namely, BDT-DPA-F, which induces the self-assembly into a fibril network that is beneficial for improved hole mobility and reduced energy disorder. With the help of additional intermolecular $C-H\cdots F$ hydrogen bonding and $F\cdots S$ dipole-dipole interactions, the as-fabricated dopant-free HTM-based n-i-p standard devices achieved a high PCE of 23.12%.^[31] However, the successful use of the attractive $F\cdots S$ dipole-dipole interactions for self-assembled dopant-free HTMs is still rare in the case of inverted LHPSCs. On the other hand, given that in inverted devices the HTMs are coated before the perovskite formation, they can influence not only the interfacial charge transfer but also the crystallization of the atop perovskite as a growth template.^[32,33] Hence, it is of importance to design a dopant-free small-molecule HTM with high charge mobility by combining a good self-assembling ability with suitable surface properties for well-grown perovskite crystals in inverted devices.

Herein, we designed a new type of conjugated small-molecule HTMs with a donor- π bridge-donor ($D-\pi-D$) linear backbone by introducing substituted triphenylamine (TPA) and 3,6-dimethoxythieno[3,2-b]thiophene as the donor (side group) and π bridge (core part), respectively, to control their intra- and intermolecular interactions for obtaining self-assembled dopant-free HTM. The first-ever proposal of multimolecular dipole-dipole interactions based on the core side groups, that is, F (side) $\cdots S$ (core), can significantly enlarge the molecular planarity for enhancing the intramolecular charge delocalization as well as the $\pi-\pi$ stacking ability. By tuning the substituted atoms on the TPA side groups, two different molecules were synthesized, namely, TPAOF (O substituents) and TPASF (S substituents). Benefiting from the sulfonation of TPA moieties, TPASF can self-assemble upon the additional $F\cdots S$ dipole-dipole interactions between the F atoms in one molecular side chain and the S atoms in another molecular side chain. We show that the hole mobility of TPASF is improved by a factor of more than 3 compared to that of TPAOF, attributed to the self-assembly-induced formation of a supramolecule-like network within the TPASF HTM. Such an ordered molecular structure is also favorable for extracting the holes and hindering the nonradiative recombination at the HTM/perovskite interface. The resultant dopant-free TPASF HTM-based inverted devices achieve a maximum PCE of 21.01%, outperforming that (19.99%) of TPAOF HTM-based

ones, which is attributed to the increase in the short-circuit current density (J_{sc}) and fill factor (FF). More importantly, our maximum power point tracking (MPPT) test under continuous 1 sun illumination confirms the outstanding photostability of TPASF HTM-based inverted devices with a T_{80} lifetime of ≈ 632 h. We attribute these outcomes to the synergistic self-assembly realized by $F\cdots S$ dipole-dipole intra- and intermolecular interactions within the TPASF HTM.

2. Results and Discussion

2.1. Design and Synthesis of Self-Assembled TPASF HTM

Figure 1a,b shows the chemical structures of TPAOF and TPASF, which contain an identical $D-\pi-D$ linear skeleton, but different substituted atoms in the TPA donors, that is, O atoms for TPAOF and S atoms for TPASF. The common core part, or so-called π linker, comprises a bithiophene unit that is rarely utilized as core material in HTM designs and two inserted methoxy groups at both ends of the core, which can address the solubility issue caused by the involvement of F atoms in the side chains. The strong electron-withdrawing characteristic of F atoms in the TPA side chains can form $F\cdots S$ dipole-dipole interaction with the S atoms afforded by the bithiophene core unit, resulting in the promotion of conjugated coplanarity and intramolecular charge delocalization. Particularly for TPASF, the S substituents in the TPA side chains could generate extra $F\cdots S$ dipole-dipole moment with the F atoms from the neighboring molecules, which not only shortens the $\pi-\pi$ stacking distance but also induces the intermolecular self-assembly behavior. The synthetic routes of the two HTMs are presented in Scheme S1, Supporting Information, and the details of the synthesis and characterization are described in the Supporting Information.

The molecular structural and elemental characterizations (see Figure S1–S8, Supporting Information) confirm the successful synthesis of targeted TPAOF and TPASF with high purity. The thermal properties of the as-synthesized HTMs were probed by the thermogravimetric analysis (TGA) (Figure S9, Supporting Information). Both HTMs show relatively good thermal stability with no obvious weight loss before 265 °C, while a 5% weight loss is detected at 290 and 299 °C for TPAOF and TPASF, respectively. Our density functional theory (DFT) calculations (Figure 1c,d) demonstrate that both TPAOF and TPASF with $F\cdots S$ dipole-dipole intramolecular interaction can lead to small dihedral angles of 16.13° and 17.32° between the TPA side chain and the core unit, which are significantly lower than the typical twisting angle of 36° between the conventional aromatic rings.^[30] This indicates that the intramolecular $F\cdots S$ dipole moment effect can effectively enhance the coplanarity of the molecules as well as realize a compact $\pi-\pi$ stacking in the vertical dimension.^[34,35]

To gain insight into the molecular packing mechanism, we further conducted the DFT calculations for the model system of two molecules. Figure 1e depicts the comparison of the simulated 2D viewing self-assembly patterns for TPAOF and TPASF. Due to the synergistic $F\cdots S$ dipole-dipole interactions, the TPASF molecules assemble into a well-defined 2D lamellar network by representing short $F\cdots S$ intramolecular (3.2–3.4 Å, Figure S10, Supporting Information) and intermolecular

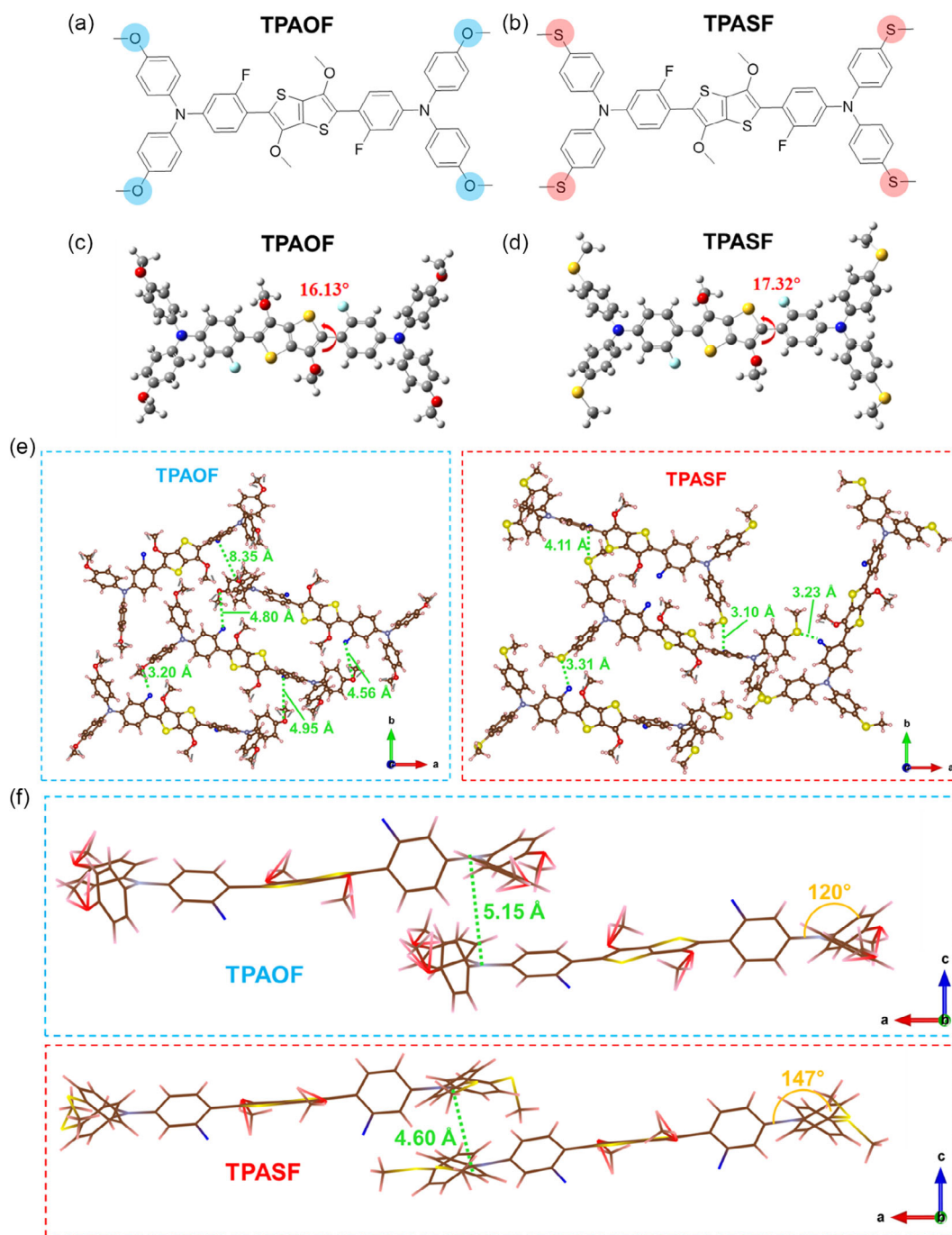


Figure 1. Chemical structures of a) TPAOF and b) TPASF. Optimized molecular structures of c) TPAOF and d) TPASF obtained at the B3LYP/6-31G* level, presenting the dihedral angles between the side group and the core unit. Simulated e) 2D viewing self-assembly mode of TPAOF (left) and TPASF (right), and f) dimerization mode of TPAOF (top) and TPASF (bottom), optimized by the DFT calculations. The green dotted lines indicate the distances of the F...O (TPAOF) and F...S (TPASF) intermolecular interactions in (e), and the dimerization distances in (f).

distances (3.1–4.1 Å). On the contrary, the TPAOF molecules form a disordered molecular arrangement with fluctuant and large F...O distances (3.2–8.4 Å) via a small van der Waals force. As presented in Figure 1f, the dimeric TPASF molecules show higher coplanarity with a larger nearby dihedral angle of 147° compared to that (120°) of the TPAOF case. Moreover, the

observed smaller dimerization distance (4.60 Å) of TPASF versus TPAOF (5.15 Å) further verifies the improved π - π packings between the TPASF molecules, which favors the self-assembling formation and the intermolecular charge transport.^[31]

To experimentally demonstrate the self-assembly behavior in the TPASF HTM, we took the atomic force microscopy (AFM)

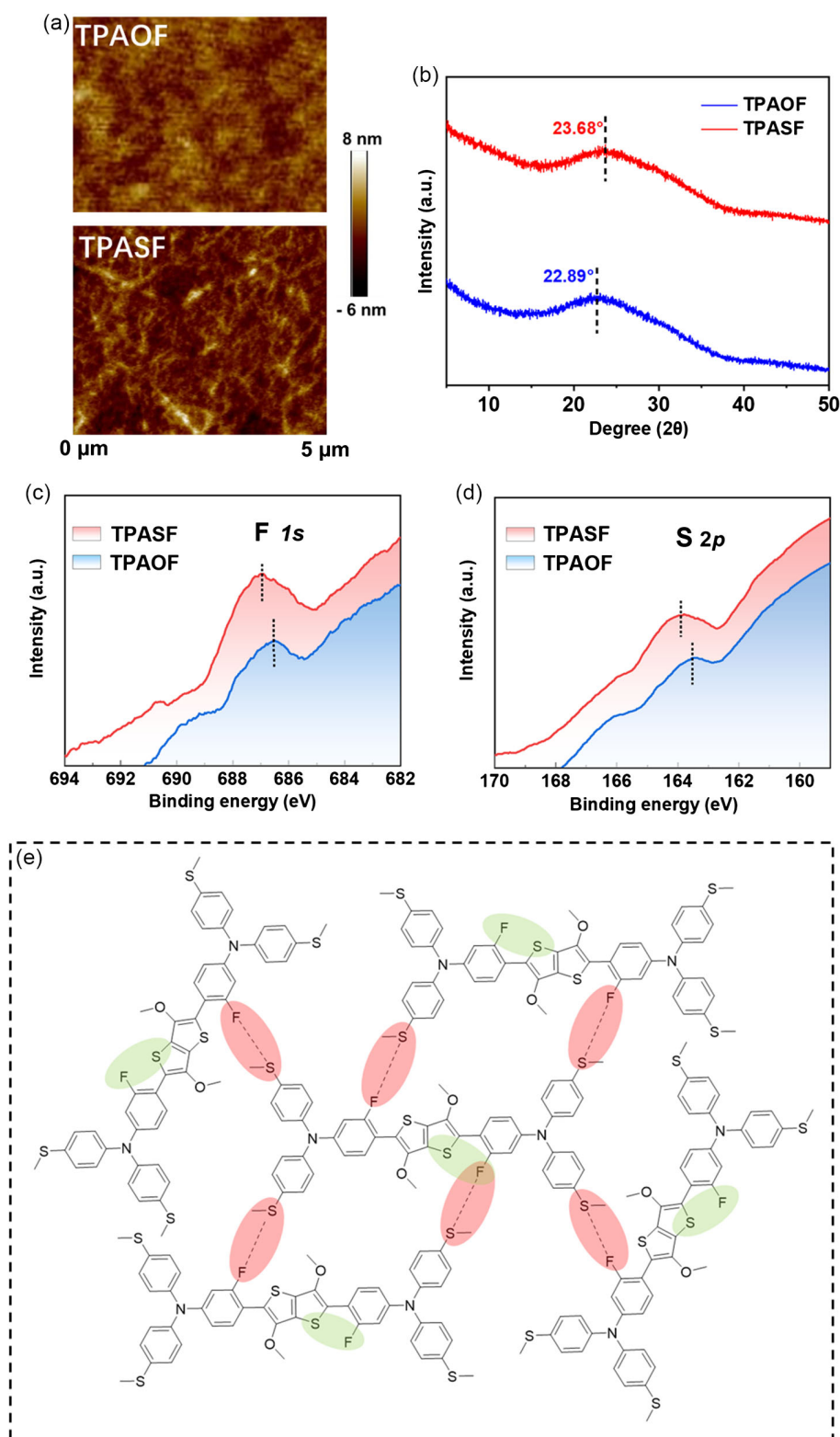


Figure 2. a) AFM images of TPAOF (top) and TPASF (bottom) films. b) XRD patterns of TPAOF and TPASF films. XPS spectra of pristine HTM films for c) F and d) S elements. e) Hypothesized arrangement of self-assembled TPASF molecules. The highlighted shadow areas in light green and red represent the possible F...S dipole-dipole intramolecular and intermolecular interactions, respectively.

images (Figure 2a), showing a fibrous morphology for the TPASF film with a slightly rough surface (roughness = 2.6 nm) while the TPAOF film with a lower surface roughness of 1.9 nm appears as an even more amorphous structure with fewer fibrils. This suggests that the self-assembly in the TPASF film indeed initiates the formation of nanofiber network, which can promote the intermolecular electron coupling for advanced hole transport properties.^[36] Moreover, the X-ray diffraction (XRD) patterns for two HTM films (Figure 2b) reveal that both molecules feature an intermolecular cofacial π - π stacking peak, located at 23.68° and 22.89° for TPASF and TPAOF, respectively, which correspond to d -spacings of 0.375 and 0.389 nm. The significantly shortened d -spacing in the case of the TPASF film suggests the stronger π - π stacking as well as molecular aggregation ability compared to the TPAOF film, benefiting from the additional intermolecular F...S dipole-dipole interactions. Our X-ray photoelectron spectroscopy (XPS) spectra (Figure 2c,d) of the pristine HTMs films further manifest the strengthened interaction of F atoms with S atoms in the case of TPASF film, attributed to the intermolecular F...S dipole moment in the neighboring molecules, situation that does not exist in the TPAOF film. The hypothesized arrangement of a self-assembled network in the TPASF HTM is presented in Figure 2e.

2.2. Optical, Electrochemical, and Hole Transport Properties

Figure 3a,b shows the comparison between the absorption spectra of TPAOF and TPASF in diluted dichloromethane solution and film state, respectively. The absorption peaks at 280–335 nm of these two small molecules are ascribed to the n - π^* transition of aniline.^[37] We also assign the exciton peaks at 377–426 nm observed partially in the visible range both in solution and in film states, to the π - π^* electron transition between the thiophene core and the weaker acceptor fluorobenzene moiety.^[38–40] Although the slightly redshifted (4 nm) first exciton peaks are observed in the solution phase (Figure 3a, Table 1), they feature distinguishable film absorption profiles by showing a significantly bathochromically shifted (34 nm) maximum absorption peak of TPASF film compared to that of TPAOF film (Figure 3b, Table 1), owing to their different assembly modes. It is worth mentioning that the absorption of TPA-based HTMs in the visible range makes a negligible effect on the light harvesting of the atop perovskite layer in inverted device structure, due to the ultrathin (<25 nm) TPA-HTM layer compared to the thick (>500 nm) perovskite layer with high absorption coefficient ($>10^5$ cm⁻¹), which will be confirmed in the following device section. Since both HTMs possess

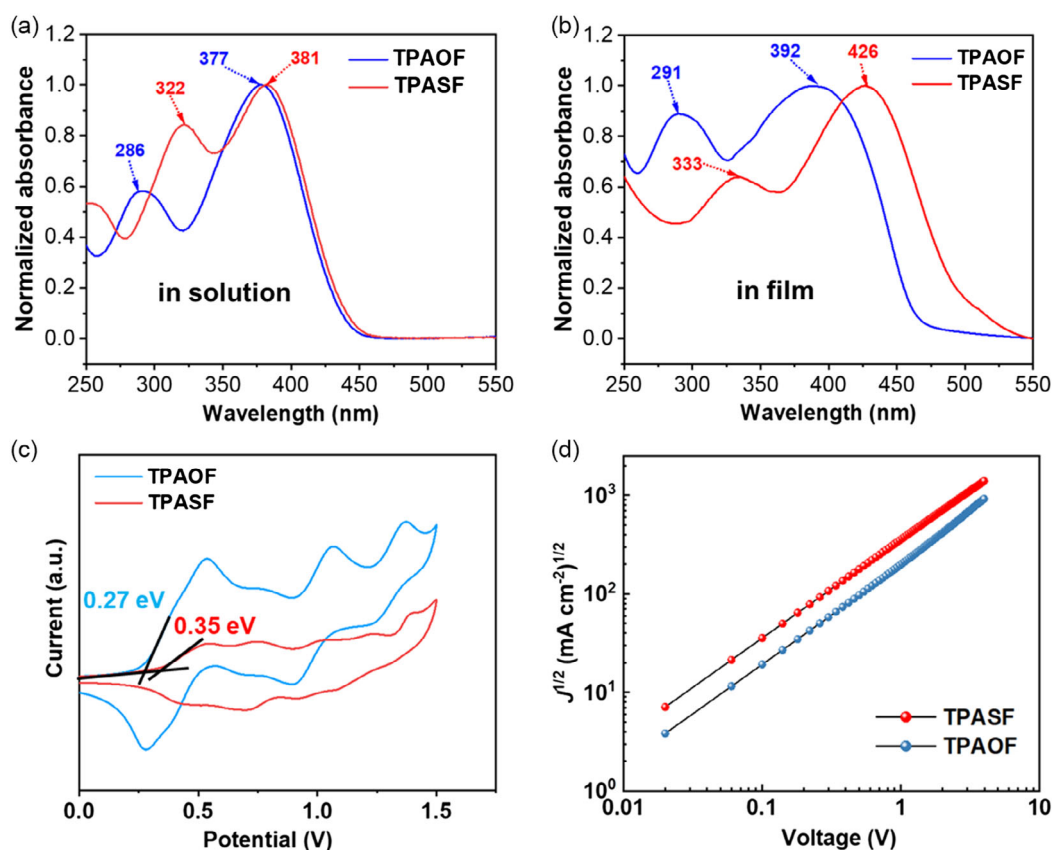


Figure 3. Normalized UV-vis absorption spectra of TPAOF and TPASF both a) in solution and b) in thin film states. c) Cyclic voltammograms of TPAOF and TPASF in dichloromethane (DCM) solution with tetrabutylammonium hexafluorophosphate (TBAPF₆, 0.1 M) as the supporting electrolyte. The oxidation potential was calculated versus ferrocene. d) Dark $J^{1/2}$ -V curves of hole-only devices with an architecture of ITO/PEDOT: PSS/HTM/MoO₃/Ag.

Table 1. Optical, electrochemical, and hole transport properties of dopant-free TPAOF and TPASF HTMs.

HTM	$\lambda_{\text{exc}}^{\text{absa)}$ [nm]		$E_{\text{HOMO}}^{\text{b)}$ [eV]	$E_{\text{LUMO}}^{\text{c)}$ [eV]	$E_{\text{g}}^{\text{optd)}$ [eV]	$\mu_{\text{h}}^{\text{e)}$ [cm ² V ^{−1} s ^{−1}]
	Solution	Thin film				
TPAOF	377	392	−5.07	−2.47	2.66	3.3×10^{-5}
TPASF	381	426	−5.15	−2.49	2.46	1.1×10^{-4}

^{a)}First exciton peak. ^{b)}HOMO levels (E_{HOMO}) are derived from CV: $-E_{\text{HOMO}} = E_{\text{onset(ox)}} + 4.8$ eV, where $E_{\text{onset(ox)}}$ is the onset potential for the oxidation versus ferrocene. ^{c)}LUMO levels (E_{LUMO}) are calculated by $E_{\text{LUMO}} = E_{\text{HOMO}} + E_{\text{g}}^{\text{opt}}$. ^{d)}Optical bandgaps ($E_{\text{g}}^{\text{opt}}$) are estimated from the onsets of the absorption spectra in film state. ^{e)}Hole mobility.

identical backbone structures except for the substituted atoms in the TPA side chains, that is, S atoms for TPASF and O atoms for TPAOF, the intermolecular F⋯S dipole–dipole interaction-induced self-assembly dramatically enhances the molecular coplanarity only within the TPASF film, which favors both the intramolecular charge delocalization and the intermolecular electron coupling.^[41] As a result of the good self-assembly ability, dopant-free TPASF demonstrates excellent hole mobility (1.1×10^{-4} cm² V^{−1} s^{−1}) that is over three times higher than that (3.3×10^{-5} cm² V^{−1} s^{−1}) of undoped TPAOF (Figure 3c, Table 1), determined from the space-charge-limited current (SCLC) measurements (see the details in the Supporting Information). Compared to the case of TPAOF, we attribute the enhanced charge transport properties in the TPASF HTM to two factors. 1) The introduction of sulfur atoms in the side groups can initiate the strong D–A effect, which is beneficial for the charge carrier transport within the molecule. 2) Due to the intermolecular F⋯S dipole–dipole interaction, the TPASF molecules exhibit a self-assembly behavior with a signature of strong aggregation, which can largely improve the intermolecular hole transport ability. We further confirm the HOMO levels of the two molecules as well as spiro-OMeTAD (see the corresponding cyclic voltammogram in Figure S11, Supporting Information) as the reference by conducting cyclic voltammetry (CV) measurements (Figure 3d), which is one key parameter to realize efficient hole extraction from perovskite to the HTMs. The derived HOMO levels for TPAOF (−5.07 eV) and TPASF (−5.15 eV) as well as the lowest unoccupied molecular orbital (LUMO) levels calculated from the optical band gaps are summarized in Table 1. It is first noted that both TPAOF and TPASF have deeper HOMO levels compared with that (−5.04 eV) of spiro-OMeTAD, achieving better energy-level alignment with the valence band (VB) (−5.57 eV) of the perovskite in this work, which will be discussed in Section 2.4. Moreover, TPASF HTM has a further deepened HOMO level compared with that of TPAOF HTM, attributed to the stronger electron-rich units related to sulfur atoms rather than oxygen atoms. TPASF also possesses a superior reducing ability that leads to its well-defined interaction with the uncoordinated lead cations at the HTM/perovskite interface.^[42]

2.3. Interfacial Charge Transfer Dynamics

To investigate the effect of the self-assembled TPASF HTM on the interfacial charge transfer dynamics, we conducted steady-state photoluminescence (PL) and time-resolved PL (TRPL)

measurements. **Figure 4a** shows the comparison between the PL spectra of glass/perovskite as a control sample and glass/HTM (TPAOF or TPASF)/ perovskite samples, excited at 460 nm. Compared with the PL amplitude of pristine perovskite (glass/perovskite), a distinguishable PL quenching was observed for both HTMs, indicating the occurrence of hole extraction from the VB of perovskite to the HOMO level of the HTMs. The TPASF HTM demonstrates an enhanced PL quenching compared to the case of TPAOF, suggesting that the self-assembly-induced ordered arrangement via the coordination of S–Pb bonding at the interface of TPASF HTM and perovskite can promote the hole extraction reaction. We then evaluated the charge separation dynamics by analyzing the TRPL decay data in Figure 4b. The hole extraction process turns out to be faster from TPAOF/perovskite to TPASF/perovskite, as evident from the observed gradual decay acceleration, which also agrees with PL quenching data. Then, a reported rate equation^[43] (see Equation (S1), Supporting Information) was used to fit the PL decays for the glass/HTM/perovskite samples, which comprises trap-associated first-order recombination, second-order recombination via nongeminate free charge carrier, and interfacial hole extraction (see the detailed analysis method in the Supporting Information). As a comparison, the PL decay for the glass/perovskite sample was fit with a simplified equation (Equation (S3), Supporting Information), which consists of only two components (first- and second-order recombination). Upon the global fitting, we extracted the first-order (k_1), second-order (k_2), and hole extraction (k_{HT}) rate constants, which are summarized in **Table 2**. The decrease in k_1 from 5.7×10^7 s^{−1} (TPAOF) to 3.8×10^7 s^{−1} (TPASF) hints that the TPASF HTM can effectively hinder the nonradiative recombination by decreasing the trap density at the HTM/perovskite interface upon the ordered coordination of S–Pb bonding. This leads to a higher hole extraction rate constant (k_{HT}) of 8.7×10^8 s^{−1} (TPASF) compared to that (4.5×10^8 s^{−1}) of TPAOF. We further described the PL decay using the differential lifetime, which has been recently employed to assess the interfacial charge transfer dynamics at the interface of perovskite and charge acceptors.^[44] The differential lifetime (τ_{PL}) can be estimated in terms of Equation (1)

$$\tau_{\text{PL}} = \left(-\frac{1}{m} \frac{\text{dln}(\phi_{\text{PL}})}{\text{dt}} \right)^{-1} \quad (1)$$

where $\phi_{\text{PL}}(t)$ is the PL intensity at t after the photoexcitation, and m is a factor in relation to the injection level, which is set as 2 for high-level injection in this work.^[44] By solving Equation (1), the

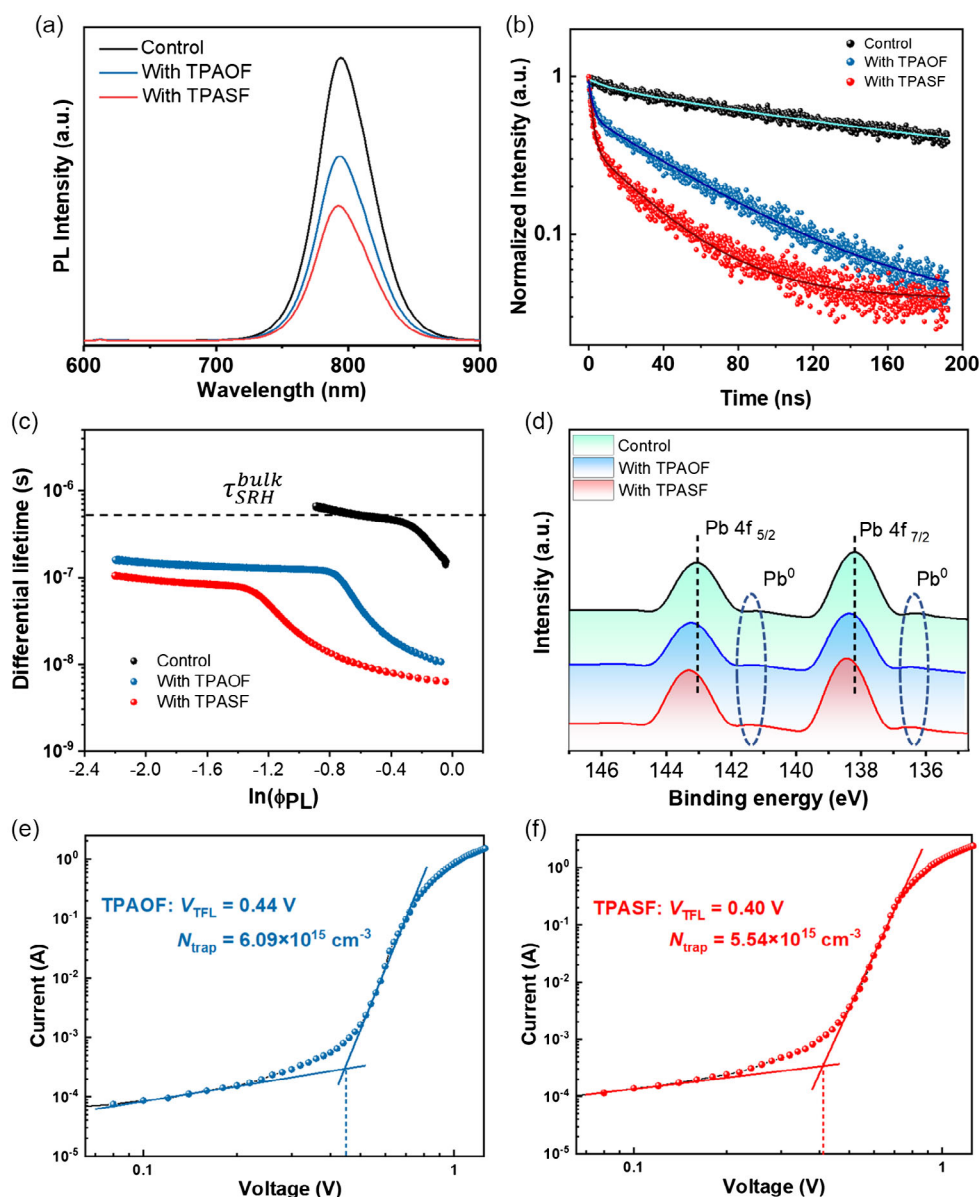


Figure 4. a) Normalized PL spectra (excited at 460 nm) and b) TRPL decays (excited at 460 nm and monitored at 785 nm) of glass/perovskite (control) and glass/HTM/perovskite films with TPAOF and TPASF, respectively. Solid lines in (b) present the fitting results with a rate law function. c) Differential lifetime versus the logarithm of the PL intensity ($\ln(\phi_{PL})$). d) XPS spectra of perovskite with and without coating on the HTMs for the core-level Pb 4f. Dark I – V curves of hole-only devices (ITO/HTM/perovskite/MoO₃/Ag) with extracted V_{TFL} kink points in perovskite films coated on e) TPAOF and f) TPASF HTMs.

Table 2. Fitting parameters of TRPL decays for the glass/HTM/perovskite films.

HTM	k_1 [s ⁻¹]	k_2 [s ⁻¹ cm ³]	k_{HT} [s ⁻¹]	Differential lifetime [ns]	Surface recombination velocity [cm s ⁻¹]
TPAOF	5.7×10^7	4.1×10^{-10}	4.5×10^8	128.3	579.8
TPASF	3.8×10^7	4.5×10^{-10}	8.7×10^8	83.7	995.2

calculated results are presented in Figure 4c by plotting τ_{PL} as a function of the logarithm of PL intensity ($\ln(\phi_{PL})$). Based on the plateau of the curve, we extracted the effective

Shockley Read Hall (SRH) lifetime in the bulk (glass/perovskite) of $\tau_{SRH}^{bulk} = 501.1$ ns, similar to the reported value for another kind of triple-cation perovskite.^[45] Thus, the effective SRH lifetimes during the hole extraction process (glass/HTM/perovskite) can be similarly evaluated as $\tau_{SRH}^{HTM} = 128.3$ ns (TPAOF) and 83.7 ns (TPASF). By taking the extracted τ_{SRH}^{bulk} and τ_{SRH}^{HTM} in Equation (2), the surface recombination velocity (S) at the HTM/perovskite interface can be calculated

$$\tau_{SRH}^{HTM} = \left(\frac{1}{\tau_{SRH}^{bulk}} + \frac{S}{2d} \right)^{-1} \quad (2)$$

where d is the perovskite layer thickness (≈ 500 nm). The higher surface recombination velocity ($S = 995.2 \text{ cm s}^{-1}$) is achieved for glass/TPASF/perovskite compared to that ($S = 579.8 \text{ cm s}^{-1}$) of the TPAOF-based sample (Table 2). The improved S in the case of TPASF further confirms the swift hole extraction and the hindering of charge recombination, benefiting from the

passivation effect of ordered S–Pb coordination at the TPASF/perovskite interface.

Our XPS study also verifies the prominent interaction of Pb^{2+} ions with the HTMs (Figure 4d). The self-assembled TPASF HTM-initiated ordered arrangement of S atoms in the side chains shows an enhanced interaction with Pb^{2+} ions, which

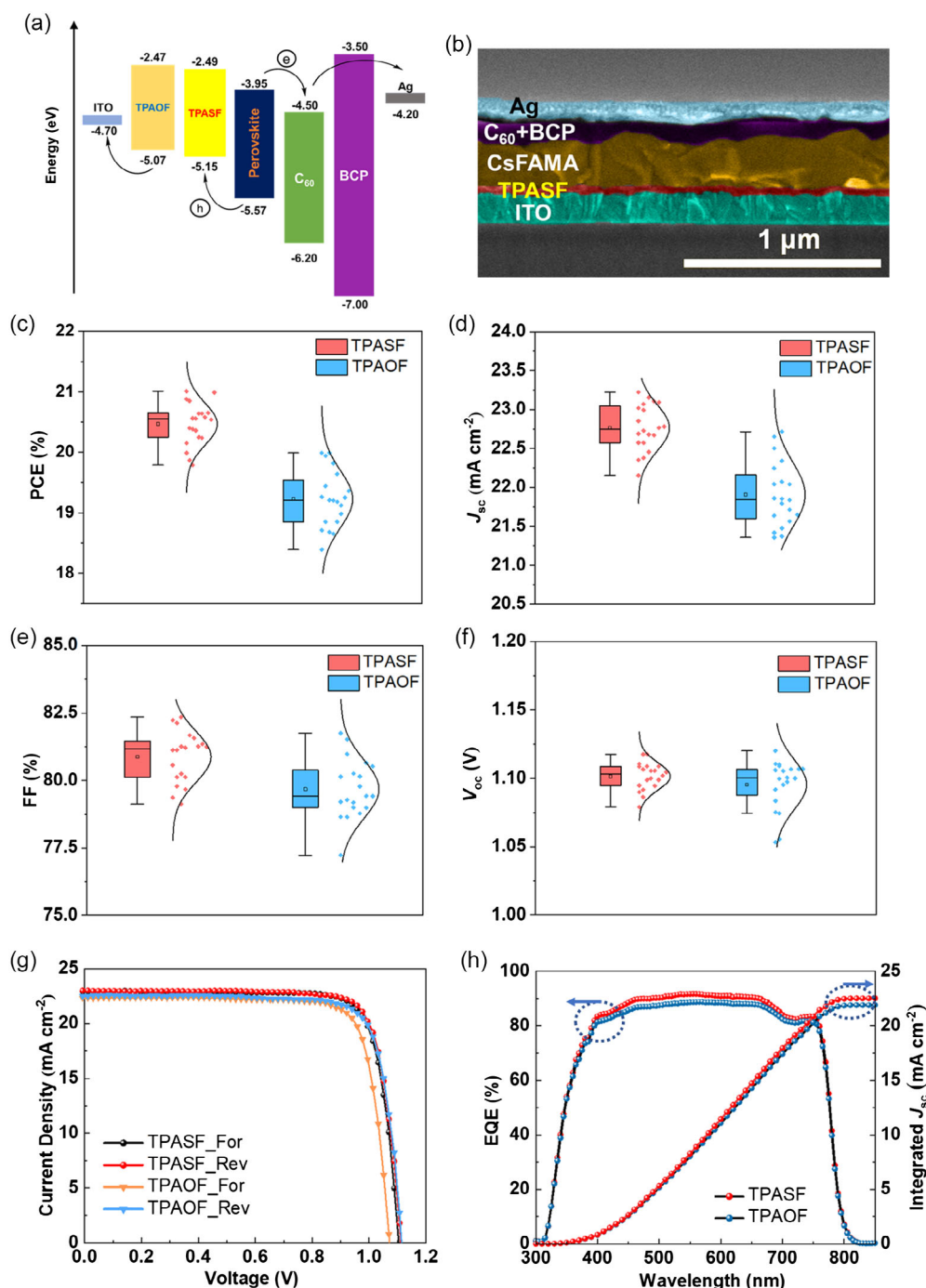


Figure 5. a) Energy-level diagram for TPAOF and TPASF HTMs and other layers of the p–i–n inverted devices. b) Cross-sectional SEM image of a typical TPASF-based solar cell with structure ITO/TPASF/CsFAMA/ C_{60} /BCP/Ag. Photovoltaic parameters of c) PCE, d) J_{sc} , e) FF, and f) V_{oc} , box charts from 20 single cells for TPAOF and TPASF, respectively. g) J–V curves and h) EQE spectra of the champion dopant-free TPAOF- and TPASF-based inverted devices.

is favorable for both defect passivation and interfacial hole transfer dynamics.^[46] Furthermore, the hole trap densities (N_{trap}) of perovskite layers coated on TPAOF (Figure 4e) and TPASF (Figure 4f) were estimated as 6.09×10^{15} and $5.54 \times 10^{15} \text{ cm}^{-3}$, respectively, which are highly consistent with the fitted k_1 ($5.7 \times 10^7 \text{ s}^{-1}$ for TPAOF and $3.8 \times 10^7 \text{ s}^{-1}$ for TPASF) from the previous PL decay data. Thus, the self-assembly feature in the TPASF molecules can not only improve the hole mobility within the HTM but also enhance the interfacial charge transfer dynamics in an ordered packing mode.

2.4. Performance of Dopant-Free TPASF HTM-Based Inverted Perovskite Solar Cells

To assess the photovoltaic performance of the dopant-free TPAOF and TPASF HTMs, p-i-n inverted LHPSCs with structure 'ITO/HTM/CsFAMA/C₆₀/BCP/Ag' (see the cell schematic in Figure 5a) were assembled (see the fabrication details in the Supporting Information). The device based on an optimized TPASF concentration of 5 mg mL^{-1} , which corresponds to a thin HTM layer of 23 nm (see the cross-sectional scanning electron microscopy (SEM) images in Figure 5b and S12, Supporting Information), exhibits an improved J_{sc} of 23.09 mA cm^{-2} , an outstanding FF of 0.82, a similar V_{oc} of 1.11 V, and a higher PCE of 21.01%, compared with those (e.g., PCE of 19.99%) derived from TPAOF devices (Figures 5c–f and Table 3). To the best of our knowledge, the 21.01% PCE is one of the highest reported values for the inverted LHPSCs with dopant-free small molecule-based HTMs (Figure S13 and S14, Supporting Information). It is noteworthy that the hysteresis (Figure 5g) is also reduced in the TPASF-based device ($\text{H-index} = 1.011$, where $\text{H-index} = \text{PCE}_{\text{rev}}/\text{PCE}_{\text{for}}$)^[47] compared with that ($\text{H-index} = 1.040$) in the case of TPAOF-based device, attributed to the reduction in the built-in electric field at the TPASF/perovskite interface since the hole can be swiftly transported through the self-assembled nanofiber network after extracting the hole.^[48] The external quantum efficiency (EQE) spectra (Figure 5h) indicate that the generation of photocurrent is mainly influenced by the interfacial charge transfer, in agreement with the improved hole extraction process for self-assembled TPASF-based devices, leading to the increase in the EQE up to over 90% compared with that ($\approx 85\%$) of TPAOF-based ones. The integrated J_{sc} values (21.9 mA cm^{-2} for TPAOF and 22.5 mA cm^{-2} for TPASF) derived from the EQE spectra are highly in line with those from the J - V curves (Table 3).

We further investigated the interfacial properties of HTMs and perovskite layer, which could make a key effect on the

performance enhancement. As compared in Figure 6a,b, the pristine TPASF film (glass/TPASF) exhibits a much lower water contact angle (80.6°) compared with that (92.5°) of TPAOF film, likely due to the more hydrophilic thiomethyl groups in the TPASF molecule rather than the methoxy unit in the TPAOF HTM. This higher wettability of TPASF film can facilitate the homogenous formation of the atop perovskite layer with the precursor dissolving in polar solvents, resulting in better crystallinity of the perovskite film with larger grain size, as evident from the estimated average perovskite crystalline grain sizes for both glass/HTM/perovskite samples (see the topographical SEM images in Figure 6c,d). In other words, the self-assembled TPASF HTM film can indeed be a good template for the perovskite growth in inverted devices. As presented in the previous XPS analysis (Figure 4d), two weak Pb^0 characteristic peaks were detected for the perovskite films with and without HTMs, indicating the existence of iodine vacancies in the perovskites.^[49] These uncoordinated iodide ions can potentially undergo complex redox reactions with HTMs, particularly at the interface area.^[50] To this end, we conducted the antioxidation test with iodine vapor fumigation. As observed in Figure 6e, after the fumigation with iodine vapor for 5 min, the fumigated area of TPAOF molecules turns to be slightly blackened color, while the TPASF remains unchanged yellowish color. We attribute the enhanced antioxidant capacity of TPASF HTM to its deeper HOMO energy level (-5.15 eV) compared with that (-5.07 eV) of TPAOF HTM,^[40] which can not only inhibit the further reduction of uncoordinated iodide ions at the HTM/perovskite interface but also prevent the active gases such as atmospheric oxygen from degrading the HTMs.

Benefiting from the advanced interfacial properties and also the high-quality perovskite layer with fewer defects, the self-assembled TPASF-based devices demonstrate high stability under continuous MPPT (1000 h) at 1 sun illumination, achieving a comparably long T_{80} lifetime of $\approx 632 \text{ h}$ (Figure 6f) with other reported T_{80} lifetimes of self-assembled HTM-based inverted devices with initially high PCEs ($>21\%$),^[20,21] whereas the TPAOF-based one can only retain 80% of its initial PCE up to about 430 h. Moreover, we conducted the solvent stability test by spin coating the mixture solvent of DMSO and DMF (v:v, 4:1) that is typically used to dissolve the perovskite precursor on top of the glass/HTM films and then compared the absorption spectra of the HTM films before and after spin coating the mixture solvent in Figure S15, Supporting Information. It is noted that upon the solvent washing the absorbances at the first exciton peaks for TPAOF (392 nm) and TPASF (426 nm) can still retain 91% and 77% of their corresponding initial values, respectively, hinting that these types of HTM molecules can effectively resist the coating or washing of the mixture solvent (DMSO/DMF), which can act as a good template for the perovskite deposition on top. Finally, the thermal stability of the devices was investigated by heating the cells at 65°C for continuous 24 h in a nitrogen-filled glove box.^[51,52] Figure S16, Supporting Information, depicts the comparison of the normalized PCEs obtained before and after heating. The TPASF-based device can retain 90.8% of its initial value recorded before heating which is higher than that (83.5%) with the TPAOF-based one, indicating that the self-assembled TPASF HTM possesses higher heating tolerance for atop perovskite compared to the disordered

Table 3. Photovoltaic parameters of dopant-free inverted LHPSCs based on TPASF and TPAOF, derived from 20 devices in each case. All presented data are acquired from the reverse scan.

HTM	V_{oc} [V]		J_{sc} [mA cm^{-2}]		FF [%]		PCE [%]	
	Best	Average	Best	Average	Best	Average	Best	Average
TPAOF	1.11	1.09	22.52	21.90	81.75	79.67	19.99	19.22
TPASF	1.11	1.10	23.09	22.79	82.35	80.88	21.01	20.46

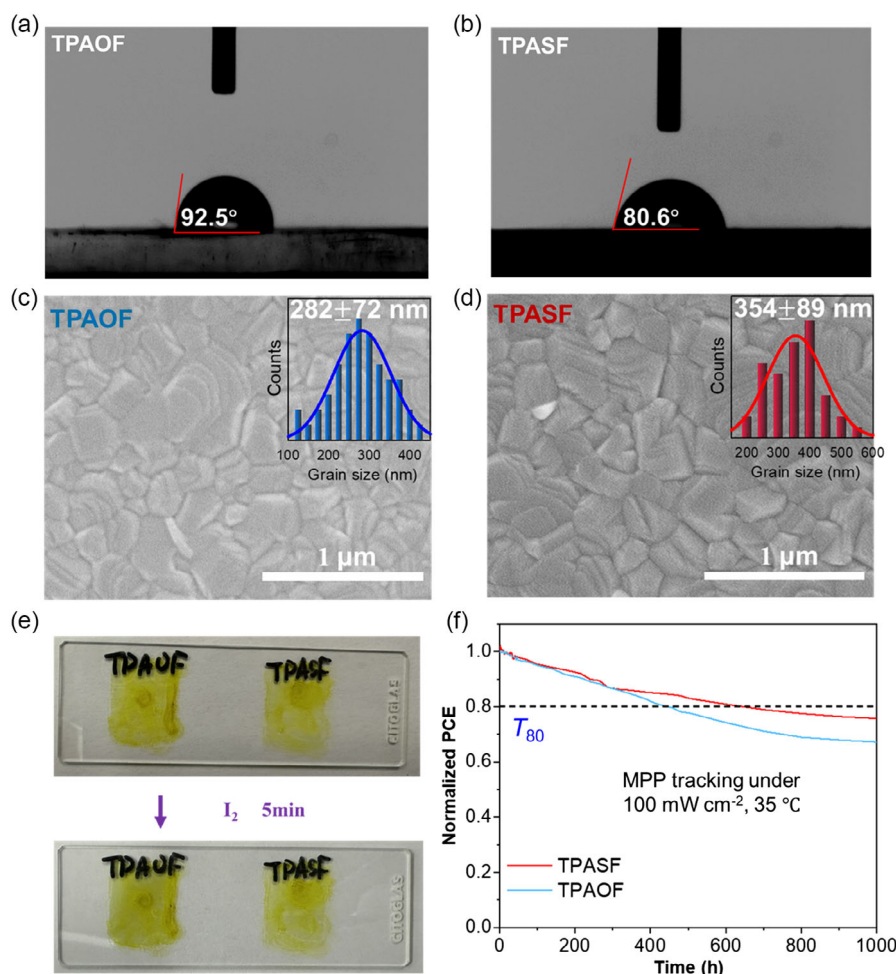


Figure 6. Water contact angles for a) TPAOF and b) TPASF films on glass. Topographical SEM images of perovskite films capped on c) TPAOF and d) TPASF HTMs. Insets in (c) and (d) show the distribution of perovskite crystalline grain size with the calculated average value. e) Color variation of TPAOF (O) and TPASF (S) films on glass substrates after exposure to I₂ vapor for 5 min. f) Comparison of normalized PCE of encapsulated TPAOF- and TPASF-based inverted devices under ambient conditions and light soaking at the MPP (1 sun illumination, 100 mW cm⁻²; 420 nm UV light cut-off filter; 35 °C).

TPAOF HTM, in other words, higher thermal stability of the corresponding device. Our results suggest that the unique self-assembly via synergistic F...S dipole-dipole intra- and intermolecular interactions within the TPASF HTM can positively tailor the interfacial properties for both performance and stability enhancement in inverted LHPSCs.

3. Conclusion

In summary, we used a molecular assembly strategy to synthesize a low-cost and dopant-free HTM (TPASF) with a distinct self-assembly behavior via the synergistic F...S dipole-dipole intra- and intermolecular interactions. The self-assembled TPASF HTM film demonstrated high molecular coplanarity, well-defined energy level, good modulation of surface properties, and favorable growth template, leading to high hole mobility, efficient interfacial charge transfer, and well-grown perovskite crystals. Such excellent inherent and interfacial properties contributed to the achievement of a high PCE of 21.01% for the

inverted LHPSCs. More importantly, the outstanding antioxidant capacity of TPASF HTM along with the high quality of perovskite layer with low trap density secured high operational stability with a long T₈₀ lifetime of ≈632 h under MPP tracking. Proposing such a simple and self-assembled HTM by precisely controlling the molecular framework will pave the way for the combination of superior charge transfer and good perovskite growth for efficient and stable inverted p-i-n devices.

Supporting Information

Supporting Information is available from the Wiley Online Library or from the author.

Acknowledgements

R.L. and J.Z. contributed equally to this work. M.L. acknowledges the Finnish Cultural Foundation (no. 00220107) for funding. H.Z. and Z.Z. acknowledge Young Taishan Scholars, P.R. China (grant nos. 201909120 and 201909121). P.V. thanks financial support of Jane and

Aatos Erkko foundation (SOL-TECH project) and Academy of Finland (decision no. 347772). This work is part of the Academy of Finland Flagship Programme, Photonics Research and Innovation (PREIN), decision no. 320165. S.K.M. and S.P.R. acknowledge the Australian government through the Australian Research Council (ARC) under the Centre of Excellence scheme (project no. CE170100026) and the computational research work was undertaken with the assistance of resources and services from the National Computational Infrastructure (NCI), which is supported by the Australian Government. S.K.M. thanks financial support from International Postdoctoral Fellowship of Japan Society for the Promotion of Science (JSPS). An equal contribution statement has been added to the Acknowledgements on 13 March 2023, after initial online publication of the Version of Record.

Conflict of Interest

The authors declare no conflict of interest.

Data Availability Statement

The data that support the findings of this study are available from the corresponding author upon reasonable request.

Keywords

dipole–dipole moments, dopant-free hole transport materials, intra- and intermolecular interactions, inverted perovskite solar cells, self-assembly

Received: January 18, 2023

Revised: February 8, 2023

Published online: March 2, 2023

- [1] NREL, <https://www.nrel.gov/pv/assets/pdfs/best-research-cell-efficiencies-rev220630.pdf> (accessed: January 2023).
- [2] F. M. Rombach, S. A. Haque, T. J. Macdonald, *Energy Environ. Sci.* **2021**, 14, 5161.
- [3] T. Zhang, F. Wang, H. B. Kim, I. W. Choi, C. Wang, E. Cho, R. Konefal, Y. Puttisong, K. Terado, L. Kobera, M. Chen, M. Yang, S. Bai, B. Yang, J. Suo, S. C. Yang, X. Liu, F. Fu, H. Yoshida, W. M. Chen, J. Brus, V. Coropceanu, A. Hagfeldt, J. L. Brédas, M. Fahlman, D. S. Kim, Z. Hu, F. Gao, *Science* **2022**, 377, 495.
- [4] J. Siekmann, S. Ravishankar, T. Kirchartz, *ACS Energy Lett.* **2021**, 9, 3244.
- [5] J. Feng, Y. Jiao, H. Wang, X. Zhu, Y. Sun, M. Du, Y. Cao, D. Yang, S. F. Liu, *Energy Environ. Sci.* **2021**, 14, 3035.
- [6] X. Zheng, B. Chen, J. Dai, Y. Fang, Y. Bai, Y. Lin, H. Wei, X. C. Zeng, J. Huang, *Nat. Energy* **2017**, 2, 17102.
- [7] F. Li, X. Deng, F. Qi, Z. Li, D. Liu, D. Shen, M. Qin, S. Wu, F. Lin, S. H. Jang, J. Zhang, X. Lu, D. Lei, C. S. Lee, Z. Zhu, A. K. Y. Jen, *J. Am. Chem. Soc.* **2020**, 142, 20134.
- [8] D. Luo, W. Yang, Z. Wang, A. Sadhanala, Q. Hu, R. Su, R. Shivanna, G. F. Trindade, J. F. Watts, Z. Xu, T. Liu, K. Chen, F. Ye, P. Wu, L. Zhao, J. Wu, Y. Tu, Y. Zhang, X. Yang, W. Zhang, R. H. Friend, Q. Gong, H. J. Snaith, R. Zhu, *Science* **2018**, 360, 1442.
- [9] X. Zheng, Y. Hou, C. Bao, J. Yin, F. Yuan, Z. Huang, K. Song, J. Liu, J. Troughton, N. Gasparini, C. Zhou, Y. Lin, D. J. Xue, B. Chen, A. K. Johnston, N. Wei, M. N. Hedhili, M. Wei, A. Y. Alsalloum, P. Maity, B. Turedi, C. Yang, D. Baran, T. D. Anthopoulos, Y. Han, Z. H. Lu, O. F. Mohammed, F. Gao, E. H. Sargent, O. M. Bakr, *Nat. Energy* **2020**, 5, 131.
- [10] C. Bi, Q. Wang, Y. Shao, Y. Yuan, Z. Xiao, J. Huang, *Nat. Commun.* **2015**, 6, 7373.
- [11] P. Yan, D. Yang, H. Wang, S. Yang, Z. Ge, *Energy Environ. Sci.* **2022**, 15, 3630.
- [12] H. D. Pham, T. T. Do, J. Kim, C. Charbonneau, S. Manzhos, K. Feron, W. C. Tsoi, J. R. Durrant, S. M. Jain, P. Sonar, *Adv. Energy Mater.* **2018**, 8, 1703007.
- [13] R. Li, C. Li, M. Liu, P. Vivo, M. Zheng, Z. Dai, J. Zhan, B. He, H. Li, W. Yang, Z. Zhou, H. Zhang, *CCS Chem.* **2021**, 4, 3084.
- [14] J. Wang, H. Shi, N. Xu, J. Zhang, Y. Yuan, M. Lei, L. Wang, P. Wang, *Adv. Funct. Mater.* **2020**, 30, 2002114.
- [15] Y. Wang, W. Chen, L. Wang, B. Tu, T. Chen, B. Liu, K. Yang, C. W. Koh, X. Zhang, H. Sun, G. Chen, X. Feng, H. Y. Woo, A. B. Djurišić, Z. He, X. Guo, *Adv. Mater.* **2019**, 31, 1902781.
- [16] Y. Cao, Y. Li, T. Morrissey, B. Lam, B. O. Patrick, D. J. Dvorak, Z. Xia, T. L. Kelly, C. P. Berlinguette, *Energy Environ. Sci.* **2019**, 12, 3502.
- [17] Y. Wang, Q. Liao, J. Chen, W. Huang, X. Zhuang, Y. Tang, B. Li, X. Yao, X. Feng, X. Zhang, M. Su, Z. He, T. J. Marks, A. Facchetti, X. Guo, *J. Am. Chem. Soc.* **2020**, 142, 16632.
- [18] N. Xu, A. Zheng, Y. Wei, Y. Yuan, J. Zhang, M. Lei, P. Wang, *Chem. Sci.* **2020**, 11, 3418.
- [19] W. Chen, Y. Wang, B. Liu, Y. Gao, Z. Wu, Y. Shi, Y. Tang, K. Yang, Y. Zhang, W. Sun, X. Feng, F. Laquai, H. Y. Woo, A. B. Djurišić, X. Guo, Z. He, *Sci. China Chem.* **2020**, 64, 41.
- [20] N. Cai, F. Li, Y. Chen, R. Luo, T. Hu, F. Lin, S. Yiu, D. Liu, D. Lei, Z. Zhu, A. K. -Y. Jen, *Angew. Chem. Int. Ed.* **2021**, 60, 20437.
- [21] Q. Liao, Y. Wang, Z. Zhang, K. Yang, Y. Shi, K. Feng, B. Li, J. Huang, P. Gao, X. Guo, *J. Energy Chem.* **2022**, 68, 87.
- [22] S. Zhang, R. Wu, C. Mu, Y. Wang, L. Han, Y. Wu, W. H. Zhu, *ACS Mater. Lett.* **2022**, 4, 1976.
- [23] F. Yang, S. Cheng, X. Zhang, X. Ren, R. Li, H. Dong, W. Hu, *Adv. Mater.* **2018**, 30, 1702415.
- [24] C. Chang, H. Huang, H. Tsai, S. Lin, P. Liu, W. Chen, F. Hsu, W. Nie, Y. Chen, L. Wang, *Adv. Sci.* **2021**, 8, 2002718.
- [25] M. Más-Montoya, P. Gómez, D. Curiel, I. Silva, J. Wang, R. A. J. Janssen, *Chem. – Eur. J.* **2020**, 26, 10276.
- [26] C. C. Robertson, J. S. Wright, E. J. Carrington, R. N. Perutz, C. A. Hunter, L. Brammer, *Chem. Sci.* **2017**, 8, 5392.
- [27] H. Zhang, R. Li, Z. Deng, S. Cui, Y. Wang, M. Zheng, W. Yang, *Dyes Pigm.* **2020**, 181, 108552.
- [28] A. Vulpatti, C. Dalvit, *Chem. – Eur. J.* **2021**, 27, 8764.
- [29] S. Li, W. Zhao, J. Zhang, X. Liu, Z. Zheng, C. He, B. Xu, Z. Wei, J. Hou, *Chem. Mater.* **2020**, 32, 1993.
- [30] Y. K. Wang, H. Ma, Q. Chen, Q. Sun, Z. Liu, Z. Sun, X. Jia, Y. Zhu, S. Zhang, J. Zhang, N. Yuan, J. Ding, Y. Zhou, B. Song, Y. Li, *ACS Appl. Mater. Interfaces* **2021**, 13, 7705.
- [31] Q. Cheng, H. Chen, F. Yang, Z. Chen, W. Chen, H. Yang, Y. Shen, X. Ou, Y. Wu, Y. Li, Y. Li, *Angew. Chem. Int. Ed.* **2022**, 61, 202210613.
- [32] L. Wan, W. Zhang, S. Fu, L. Chen, Y. Wang, Z. Xue, Y. Tao, W. Zhang, W. Song, J. Fang, *J. Mater. Chem. A* **2020**, 8, 6517.
- [33] X. Sun, X. Deng, Z. Li, B. Xiong, C. Zhong, Z. Zhu, Z. Li, A. K. -Y. Jen, *Adv. Sci.* **2020**, 7, 1903331.
- [34] X. Kong, Y. Jiang, X. Wu, C. Chen, J. Guo, S. Liu, X. Gao, G. Zhou, J. M. Liu, K. Kempa, J. Gao, *J. Mater. Chem. A* **2020**, 8, 1858.
- [35] Z. Li, Y. Tong, J. Ren, Q. Sun, Y. Tian, Y. Cui, H. Wang, Y. Hao, C. S. Lee, *Chem. Eng. J.* **2020**, 402, 125923.
- [36] R. Kaneko, T. H. Chowdhury, K. Sugawa, J. J. Lee, J. Otsuki, A. Islam, *Sol. Energy* **2019**, 194, 248.
- [37] F. Zhang, X. Zhao, C. Yi, D. Bi, X. Bi, P. Wei, X. Liu, S. Wang, X. Li, S. M. Zakeeruddin, M. Grätzel, *Dyes Pigm.* **2017**, 136, 273.
- [38] H. D. Pham, H. Hu, K. Feron, S. Manzhos, H. Wang, Y. M. Lam, P. Sonar, *Sol. RRL* **2017**, 1, 1700105.

- [39] K. Yang, Q. Liao, J. Huang, Z. Zhang, M. Su, Z. Chen, Z. Wu, D. Wang, Z. Lai, H. Y. Woo, Y. Cao, P. Gao, X. Guo, *Angew. Chem. Int. Ed.* **2022**, 61, 202113749.
- [40] X. Yu, Z. Li, X. Sun, C. Zhong, Z. Zhu, Z. Li, A. K. Y. Jen, *Nano Energy* **2021**, 82, 105701.
- [41] K. Yang, Q. Liao, J. Huang, Z. Zhang, M. Su, Z. Chen, Z. Wu, D. Wang, Z. Lai, H. Y. Woo, Y. Cao, P. Gao, X. Guo, *Angew. Chem.* **2022**, 134, 202113749.
- [42] R. Li, M. Liu, S. K. Matta, A. Hiltunen, Z. Deng, C. Wang, Z. Dai, S. P. Russo, P. Vivo, H. Zhang, *Adv. Sustainable Syst.* **2021**, 5, 2100244.
- [43] M. Liu, M. Endo, A. Shimazaki, A. Wakamiya, Y. Tachibana, *ACS Appl. Energy Mater.* **2018**, 1, 3722.
- [44] L. Krückemeier, B. Krogmeier, Z. Liu, U. Rau, T. Kirchartz, *Adv. Energy Mater.* **2021**, 11, 2003489.
- [45] M. Liu, S. Dahlström, C. Ahläng, S. Wilken, A. Degterev, A. Matuhina, M. Hadadian, M. Markkanen, K. Aitola, A. Kamppinen, J. Deska, O. Mangs, M. Nyman, P. D. Lund, J.-H. Smått, R. Österbacka, P. Vivo, *J. Mater. Chem. A* **2022**, 10, 11721.
- [46] S. Gharibzadeh, P. Fassi, I. M. Hossain, P. Rohrbeck, M. Frericks, M. Schmidt, T. Duong, M. R. Khan, T. Abzieher, B. A. Nejand, F. Schackmar, O. Almora, T. Feeney, R. Singh, D. Fuchs, U. Lemmer, J. P. Hofmann, S. A. L. Weber, U. W. Paetzold, *Energy Environ. Sci.* **2021**, 14, 5875.
- [47] L. Canil, J. Salunke, Q. Wang, M. Liu, H. Köbler, M. Flatken, L. Gregori, D. Meggiolaro, D. Ricciarelli, F. De Angelis, M. Stolterfoht, D. Neher, A. Priimagi, P. Vivo, A. Abate, *Adv. Energy Mater.* **2021**, 11, 2101553.
- [48] C. Wang, M. Liu, S. Rahman, H. P. Pasanen, J. Tian, J. Li, Z. Deng, H. Zhang, P. Vivo, *Nano Energy* **2022**, 101, 107604.
- [49] C. Mai, Q. Zhou, Q. Xiong, C. Chen, J. Xu, Z. Zhang, H. Lee, C. Yeh, P. Gao, *Adv. Funct. Mater.* **2021**, 31, 2007762.
- [50] X. Sun, F. Wu, C. Zhong, L. Zhu, Z. Li, *Chem. Sci.* **2019**, 10, 6899.
- [51] S. Valero, S. Collavini, S. F. Völker, M. Saliba, W. R. Tress, S. M. Zakeeruddin, M. Grätzel, J. L. Delgado, *Macromolecules* **2019**, 52, 2243.
- [52] H. Zhang, M. Liu, W. Yang, L. Judin, T. I. Hukka, A. Priimagi, Z. Deng, P. Vivo, *Adv. Mater. Interfaces* **2019**, 6, 1901036.